Efficient Full Waveform Inversion Subject To A Total Variation Constraint

Yudai INADA
Institute of Science Tokyo
inada.y.af@m.titech.ac.jp

Shingo TAKEMOTO
Institute of Science Tokyo
takemoto.s.af@m.titech.ac.jp

Shunsuke ONO
Institute of Science Tokyo
ono@c.titech.ac.jp

Abstract—**This paper proposes an efficient algorithm for solving the total variation (TV)-constrained full waveform inversion (FWI) problem, a powerful technique for reconstructing subsurface properties from observed seismic data. Since FWI is an ill-posed inverse problem, appropriate regularizations or constraints are effective approaches to achieve accurate reconstruction. In particular, the TV-type constraint is widely known as a powerful prior that models the piecewise smoothness of subsurface properties. However, the optimization problem of the TV-type constrained FWI is difficult to solve due to the nonlinearity of the observation process and the non-smoothness of the TV-type constraint. Conventional approaches to solve the FWI problem rely on inner loops and/or approximations, leading to high computational cost and/or inappropriate solutions. To address these challenges, we develop an efficient algorithm with neither inner loops nor approximations to solve the FWI problem based on a primal-dual splitting method. We also demonstrate the effectiveness of the proposed method through experiments using the SEG/EAGE Salt and Overthrust Models.**

Index Terms—**full waveform inversion, total variation, primal-dual splitting method.**

I. INTRODUCTION

Full waveform inversion (FWI) [1, 2] is a technique used to reconstruct subsurface properties from seismic data recorded at multiple observation points. These subsurface properties play a crucial role in geological research and resource exploration, including investigations into gas, oil, mineral, and groundwater [2–4]. Beyond geological applications, FWI has also been successfully applied to non-destructive testing in medical and industrial fields [5, 6].

A major challenge in FWI arises from the nonlinear and complex nature of the observation process [2], which makes a direct analytical inverse solution impossible. Consequently, FWI is typically formulated as an optimization problem [1, 7–12], such as minimizing the squared error between observed and simulated seismic data. However, since FWI is ill-posed, researchers often incorporate Tikhonov [13] or total variation (TV)-type [14, 15] regularizations to promote piecewise smoothness in the reconstructed subsurface properties [16–20]. While these approaches are effective, they require careful tuning of a balance parameter that weights the data fidelity term against the regularization term. An alternative strategy is to incorporate the TV prior as a constraint, rather than using it as a regularization term [21–24]. This formulation has the advantage of allowing the parameter for the TV constraint to be determined independently of the objective function value,

relying instead on prior knowledge of subsurface properties [25–30]. This approach facilitates a more straightforward interpretation of both the formulation and the reconstructed subsurface properties.

Despite these advantages, solving the TV-constrained FWI problem remains challenging due to the combination of nonlinear forward modeling and the non-smoothness of the TV term. Conventional methods [21–24] typically include an inner loop to enforce the constraint at each optimization step, which significantly increases the computational cost. Moreover, they often rely on approximations, such as linear or quadratic approximation and enforce the constraint outside the main optimization method, potentially degrading the reconstruction accuracy.

In this paper, we propose a novel algorithm to solve the TV constrained FWI problem based on the primal-dual splitting (PDS) method. Our algorithm addresses the challenges posed by both the nonlinearity of the observation process and the non-smoothness of the TV constraint without approximations, resulting in a more accurate reconstruction. Moreover, by handling the constraint without inner loops, our algorithm is significantly more efficient compared to existing methods. Through numerical experiments on the SEG/EAGE Salt and Overthrust Models, we demonstrate that our method outperforms existing approaches in terms of both efficiency and accuracy.

II. PRELIMINARIES

A. Mathematical Tools

Throughout this paper, we denote vectors and matrices by bold lowercase letters (e.g., $\boldsymbol{x}$) and bold uppercase letters (e.g., $\boldsymbol{X}$), respectively.

For $\boldsymbol{x} \in \mathbb{R}^{\mathrm{N}}$, the mixed $l_{1,2}$ norm is defined as follows:

$$\|\boldsymbol{x}\|_{1,2} \coloneqq \sum_{\mathfrak{g} \in \mathfrak{G}} \|\boldsymbol{x}_{\mathfrak{g}}\|_2, \tag{1}$$

where $\mathfrak{G}$ is a set of disjoint index sets, and $\boldsymbol{x}_{\mathfrak{g}}$ is the subvector of $\boldsymbol{x}$ indexed by $\mathfrak{g}$.

For $\boldsymbol{x} \in \mathbb{R}^{\mathrm{N}}$, the total variation (TV) [14] is defined as follows:

$$\mathrm{TV}(\boldsymbol{x}) \coloneqq \|\mathbf{D}\boldsymbol{x}\|_{1,2} = \sum_{i=1}^{\mathrm{N}} \sqrt{d_{h,i}^2 + d_{v,i}^2}, \tag{2}$$

where $d_{h,i}$ and $d_{v,i}$ are the horizontal and vertical differences of the i-th element of $\boldsymbol{x}$, respectively, when the vector $\boldsymbol{x}$ is considered as a matrix.

B. Proximal Tools

We denote by $\Gamma_0(\mathbb{R}^N)$ the set of proper lower-semicontinuous convex functions $\mathbb{R}^N \to (-\infty, \infty]$.

For $\gamma > 0$ and $f \in \Gamma_0(\mathbb{R}^N)$, the proximity operator is defined as follows:

$$\text{prox}_{\gamma f}(\boldsymbol{x}) := \underset{\boldsymbol{y} \in \mathbb{R}^N}{\text{argmin}} \left\{ f(\boldsymbol{y}) + \frac{1}{2\gamma} \|\boldsymbol{y} - \boldsymbol{x}\|_2^2 \right\}. \quad (3)$$

For $f \in \Gamma_0(\mathbb{R}^N)$, the convex conjugate function f^* is defined as follows:

$$f^*(\boldsymbol{x}) := \sup_{\boldsymbol{y} \in \mathbb{R}^N} \left\{ \boldsymbol{y}^T \boldsymbol{x} - f(\boldsymbol{y}) \right\}. \quad (4)$$

The proximity operator for the convex conjugate function is expressed as follows [31, Theorem 3.1 (ii)]:

$$\text{prox}_{\gamma f^*}(\boldsymbol{x}) = \boldsymbol{x} - \gamma \text{prox}_{\frac{1}{\gamma} f} \left(\frac{1}{\gamma} \boldsymbol{x} \right). \quad (5)$$

For a nonempty closed convex set $C \subset \mathbb{R}^N$, the indicator function $\iota_C : \mathbb{R}^N \to (-\infty, \infty]$ is defined as follows:

$$\iota_C(\boldsymbol{x}) := \begin{cases} 0 & \text{if } \boldsymbol{x} \in C, \\ \infty & \text{otherwise.} \end{cases} \quad (6)$$

The proximity operator of ι_C is the projection onto C, given by

$$\text{prox}_{\gamma \iota_C}(\boldsymbol{x}) = P_C(\boldsymbol{x}) := \underset{\boldsymbol{y} \in C}{\text{argmin}} \|\boldsymbol{y} - \boldsymbol{x}\|_2. \quad (7)$$

C. Primal-Dual Splitting Algorithm

The Primal-Dual Splitting algorithm (PDS) [32–35] is applied to the following problem:

$$\min_{\boldsymbol{x} \in \mathbb{R}^N} \left\{ f(\boldsymbol{x}) + g(\boldsymbol{x}) + h(\boldsymbol{L}\boldsymbol{x}) \right\}, \quad (8)$$

where $\boldsymbol{L} \in \mathbb{R}^{M \times N}$, f is a differentiable convex function and g, h are convex functions whose proximity operator can be computed efficiently.

PDS solves Prob. (8) by iteratively updating the following:

$$\left| \begin{array}{l} \boldsymbol{x}^{(k+1)} = \text{prox}_{\gamma_1 g} \left(\boldsymbol{x}^{(k)} - \gamma_1 (\nabla f(\boldsymbol{x}^{(k)}) + \boldsymbol{L}^T \boldsymbol{y}^{(k)}) \right), \\ \boldsymbol{y}^{(k+1)} = \text{prox}_{\gamma_2 h^*} \left(\boldsymbol{y}^{(k)} + \gamma_2 \boldsymbol{L}(2\boldsymbol{x}^{(k+1)} - \boldsymbol{x}^{(k)}) \right), \end{array} \right. \quad (9)$$

where $\gamma_1, \gamma_2 \in \mathbb{R}$ are step sizes.

D. Full Waveform Inversion

Typically, FWI is treated as an optimization problem as follows[1]:

$$\underset{\boldsymbol{m} \in \mathbb{R}^N}{\text{argmin}} \quad E(\boldsymbol{m}) = \frac{1}{2} \|\boldsymbol{u}_{\text{obs}} - \boldsymbol{u}_{\text{cal}}(\boldsymbol{m})\|_2^2, \quad (10)$$

where $\boldsymbol{m} \in \mathbb{R}^N$ is the velocity model representing subsurface properties, $\boldsymbol{u}_{\text{obs}} \in \mathbb{R}^M$ is the observed seismic data, $\boldsymbol{u}_{\text{cal}} : \mathbb{R}^N \to \mathbb{R}^M$ is the observation process, and $\boldsymbol{u}_{\text{cal}}(\boldsymbol{m})$ is the
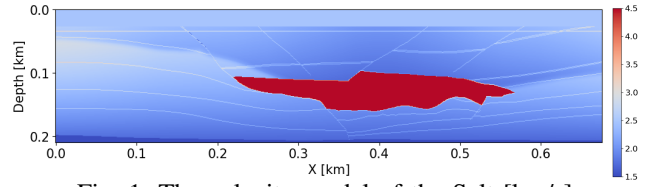

Fig. 1: The velocity model of the Salt [km/s]

modeled seismic data with the velocity model. The number of grid points is N, and the number of observed signals is M.

The observation process $\boldsymbol{u}_{\text{cal}}$ is nonlinear and complex, making it difficult to analytically derive the optimal solution. However, the gradient ∇E can be computed numerically by simulating the wave equation using the adjoint-state method [36].

III. PROPOSED METHOD

We introduce the TV and box constraint into the FWI problem to achieve more accurate reconstruction. As shown in Fig. 1, the velocity model is piecewise smooth, thus introducing the TV constraint to achieve a more accurate reconstruction. The box constraint ensures that the velocity model remains within valid ranges.

The optimization problem of the TV and box constrained FWI is formulated as follows:

$$\underset{\boldsymbol{m} \in \mathbb{R}^N}{\text{argmin}} \quad E(\boldsymbol{m}) \quad \text{s.t.} \quad \begin{cases} \|\mathbf{D}\boldsymbol{m}\|_{1,2} \leq \alpha, \\ \boldsymbol{m} \in [l, u]^N, \end{cases} \quad (11)$$

where $\alpha \in \mathbb{R}$ is the upper bound of the $l_{1,2}$ norm, and $l, u \in \mathbb{R}$ are the lower and upper bounds of the velocity model values, respectively. By incorporating TV as a constraint, the parameter α can be determined independently of other terms or constraints, which has been highlighted as an advantage in prior works [25–30]. This separation makes it possible to directly control smoothness according to α, providing a clearer interpretation of the reconstructed subsurface properties.

The constraints can be incorporated into the objective function as indicator functions:

$$\underset{\boldsymbol{m} \in \mathbb{R}^N}{\text{argmin}} \quad E(\boldsymbol{m}) + \iota_{B_{\text{box}}}(\boldsymbol{m}) + \iota_{B_{l_{1,2}}}(\mathbf{D}\boldsymbol{m}), \quad (12)$$

where

$$\begin{aligned} B_{\text{box}} &:= [l, u]^N, \\ B_{l_{1,2}} &:= \{\|\cdot\|_{1,2} \leq \alpha\}. \end{aligned} \quad (13)$$

The proximity operator of $\iota_{B_{\text{box}}}$ and $\iota_{B_{l_{1,2}}}$ can be computed efficiently. Therefore, these functions of E, $\iota_{B_{\text{box}}}$ and $\iota_{B_{l_{1,2}}}$ correspond to f, g and h in (8), respectively, $\mathbf{D}$ is corresponds to $\boldsymbol{L}$, so the problem (12) can be solved using PDS. We show the detailed algorithm in Algorithm 1.

The proximity operators of $\iota_{B_{\text{box}}}$, $\iota_{B_{l_{1,2}}}$, that is, the projection onto B_{box} and $B_{l_{1,2}}$ are calculated by

$$P_{B_{\text{box}}}(\boldsymbol{x}) = \min(\max(\boldsymbol{x}, l), u), \quad (14)$$

$$(P_{B_{l_{1,2}}}(\boldsymbol{x}))_{\mathfrak{g}_i} = \begin{cases} 0 & \text{if } \|\boldsymbol{x}_{\mathfrak{g}_i}\|_2 = 0, \\ \beta_i \frac{\boldsymbol{x}_{\mathfrak{g}_i}}{\|\boldsymbol{x}_{\mathfrak{g}_i}\|_2} & \text{otherwise,} \end{cases} \quad (15)$$

Algorithm 1 PDS for (12)

Input: $\boldsymbol{m}^{(0)}, \boldsymbol{y}^{(0)}, \gamma_0 > 0, \gamma_1 > 0$
1: **while** A stopping criterion is not satisfied **do**
2: $\quad \widetilde{\boldsymbol{m}} \leftarrow \boldsymbol{m}^{(k)} - \gamma_1 \left(\nabla E(\boldsymbol{m}^{(k)}) + \boldsymbol{D}^T \boldsymbol{y}^{(k)} \right)$
3: $\quad \boldsymbol{m}^{(k+1)} \leftarrow P_{B_{\text{box}}} \left(\widetilde{\boldsymbol{m}} \right)$
4: $\quad \widetilde{\boldsymbol{y}} \leftarrow \boldsymbol{y}^{(k)} + \gamma_2 \boldsymbol{D} \left(2\boldsymbol{m}^{(k+1)} - \boldsymbol{m}^{(k)} \right)$
5: $\quad \boldsymbol{y}^{(k+1)} \leftarrow \widetilde{\boldsymbol{y}} - \gamma_2 P_{B_{l_{1,2}}} \left(\frac{1}{\gamma_2} \widetilde{\boldsymbol{y}} \right)$
6: **end while**
Output: $\boldsymbol{m}^{(k)}$

where

$$\boldsymbol{\beta} = P_{\{\|\cdot\|_1 \le \alpha\}} \left([\|\boldsymbol{x}_{\mathfrak{g}_1}\|_2, \ldots, \|\boldsymbol{x}_{\mathfrak{g}_N}\|_2]^T \right),$$

and $\mathfrak{g}_i$ is an index set corresponding to the horizontal and vertical differences of the i-th element of $\boldsymbol{m}$.

The proximity operator for the l_1 norm upper bound constraint is expressed as follows [37]:

$$P_{\{\|\cdot\|_1 \le \alpha\}}(\boldsymbol{x}) = \text{SoftThrethold}(\boldsymbol{x}, \beta), \qquad (16)$$

where

$$\boldsymbol{x}_{\text{abs}} = \text{abs}(\boldsymbol{x}),$$
$$\boldsymbol{y} = \text{sort}_{\text{desc}}(\boldsymbol{x}_{\text{abs}}),$$
$$\beta' = \max \left\{ \frac{1}{i} \left(\left(\sum_{j=1}^{i} \boldsymbol{y}_j \right) - \alpha \right) \middle| i = 1, \ldots, N \right\},$$
$$\beta = \max \left\{ \beta', 0 \right\}.$$

Our algorithm can incorporate the constraints without requiring any approximations. Furthermore, since our algorithm can solve the TV and box constrained FWI problem without inner loops, it can be executed efficiently. In fact, the incorporation of the constraints does not significantly increase the overall computational cost, because it is fast enough compared to the ∇E computation, which requires simulation of the wave equation along the time axis.

IV. EXPERIMENTS

A. Experimental Setup

To demonstrate the effectiveness of the TV and box constrained FWI, we conducted FWI experiments where we compared with the standard FWI method[1][1], using the SEG/EAGE Salt and Overthrust Models.

The velocity model consists of 51×101 grid points. The ground truth velocity model is generated by zooming and cropping Fig. 2. The initial velocity model is generated by smoothing the ground truth velocity model with a Gaussian function with a standard deviation of 80. The source waveform is a Ricker wavelet with a peak wavelet frequency of 10 Hz. The number of waveform sources and receivers is 20 and

The standard FWI method uses the following procedures:

[1]
$$\boldsymbol{m}^{(k+1)} = \boldsymbol{m}^{(k)} - \gamma \left(\nabla E(\boldsymbol{m}^{(k)}) \right), \qquad (17)$$

where γ is the step size.
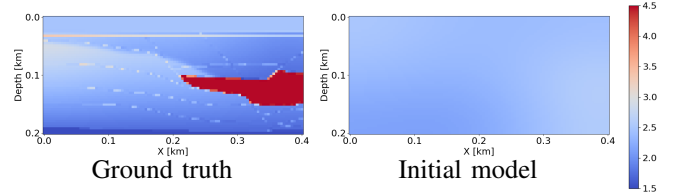
Ground truth   Initial model
Fig. 2: subsurface properties for experiments

Seismic Data   Noise Added Seismic Data
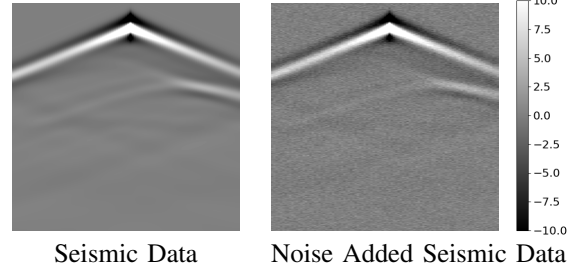Fig. 3: sinthesized seismic data

101, respectively, and they are placed on the surface at equal intervals. The gradient ∇E is computed numerically using the Devito framework[38]. The number of iterations is set to 5000. Experiments are conducted with and without noise in the observed data, as shown in Fig. 3. The noise is Gaussian noise with mean 0 and variance 1. In our algorithm, the step sizes γ_1 and γ_2 are set to 1.0×10^{-4} and 1.0×10^{2}, respectively. The lower and upper bounds of the velocity model l, u are set to 1.5[km/s] and 4.5[km/s], respectively. The experiments are conducted using α values ranging from 100 to 700 in steps of 50, representing the upper bound of the $l_{1,2}$ norm. In the standard FWI method, the step size γ is set to 1.0×10^{-4}.

B. Results and Discussion

First, we present the experimental results without noise in the observed seismic data. Fig. 4 shows the reconstructed velocity models using the standard FWI method and the proposed methods with $\alpha = 150, 350$, and 550. The standard FWI method generates wave-like artifacts throughout. In contrast, our proposed method with the best parameter, which is $\alpha = 350$, achieves the accurate velocity model reconstruction without these artifacts. The case of $\alpha = 150, 550$ will be discussed later.

For quantitative evaluation, we plot the Structural Similarity Index Measure (SSIM) against the number of iterations for our proposed method and the standard FWI method in Fig. 6. The proposed method consistently achieves higher SSIM values than the standard FWI method at every iteration, indicating enhanced reconstruction accuracy.

Second, we present the experimental results with the noisy observed seismic data. Fig. 5 shows the reconstructed velocity models using the standard FWI method and the proposed methods with $\alpha = 150, 350$ and 550. In the FWI problem with the noisy observed seismic data, the standard FWI method generates stronger wave-like artifacts throughout. In contrast, our proposed method with appropriate parameters still achieves
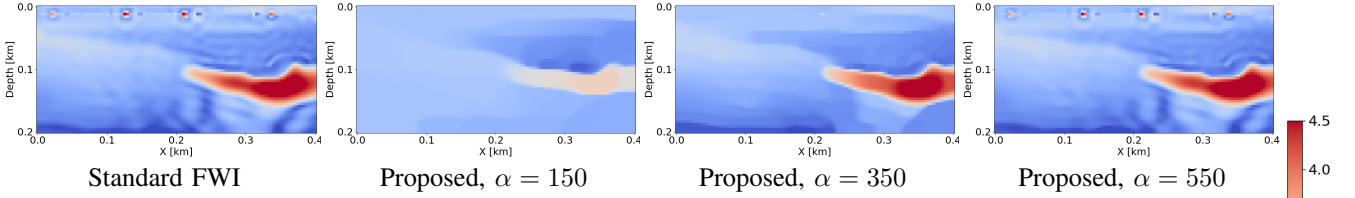
Fig. 4: Velocity models [km/s] and their corresponding reconstructions.
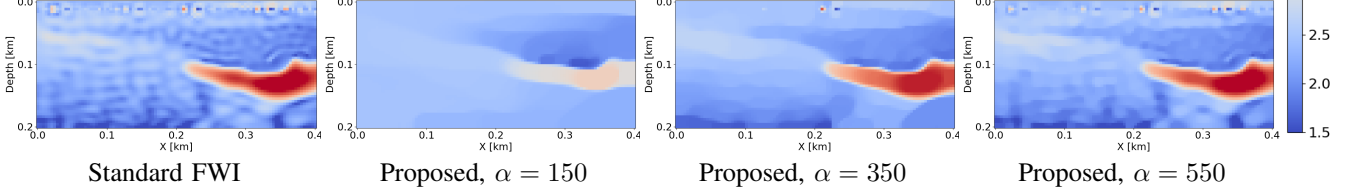

Fig. 5: Velocity models [km/s] and their corresponding reconstructions. (with the noisy data)
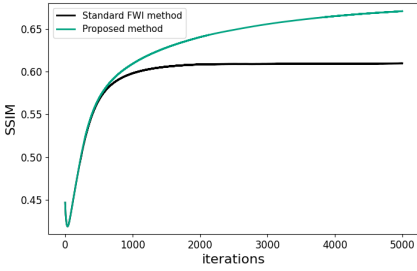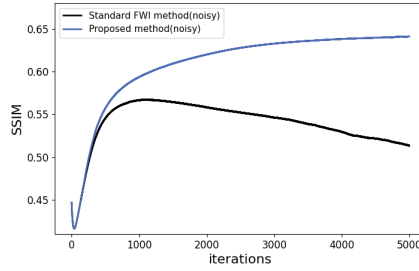

Fig. 6: SSIM against iters.

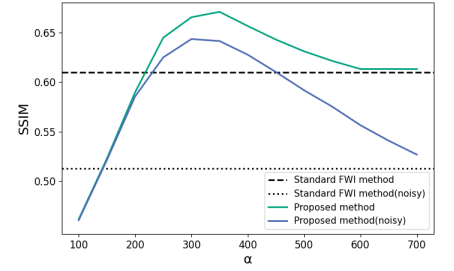

Fig. 7: SSIM against iters. (noisy)

Fig. 8: SSIM against α.

accurate velocity model reconstruction without these artifacts and achieves almost the same level of performance as in the no-noise case. This demonstrates the robustness of the reconstruction accuracy to noise in the observed seismic data.

We also plot the SSIM against the number of iterations for our proposed method and the standard FWI method in Fig. 7. The standard FWI method degrades the SSIM after a certain number of iterations. On the other hand, the proposed method maintains a consistently high value without degrading the SSIM even after a large number of iterations, indicating enhanced reconstruction accuracy.

For a more detailed analysis of the TV constraint parameter α, we plot the SSIM of our proposed method against the parameter α and the standard FWI method in Fig. 8. When $\alpha = 350$ or so, the proposed method achieves the best SSIM. As α is smaller, meaning the TV constraint becomes stronger, the SSIM worsens. On the other hand, when α becomes too large, the SSIM of our proposed method is similar to that of the standard FWI method. However, thanks to the box constraint, the proposed method still outperforms the standard FWI method. This demonstrates that the parameter α has a clear and predictable effect on the reconstructed velocity model, which can be easily adjusted to achieve accurate results. Specifically, it can be observed in Fig. 4, Fig. 5 that for $\alpha = 150$, the TV constraint is too strong, resulting in excessive smoothing, and for $\alpha = 550$, the constraint has little effect, yielding results similar to those of the standard FWI method.

V. CONCLUSION

In this paper, we developed an efficient algorithm to solve the TV and box constrained FWI problem based on PDS. Our algorithm does not require approximations when incorporating the constraints, leading to more accurate reconstructions. Furthermore, the algorithm significantly enhances computational efficiency without inner loops. Experimental results demonstrate that our method successfully eliminates wave-like artifacts and noise present in the standard FWI method, resulting in a more accurate velocity model and a higher SSIM value regardless of the presence of noise in the observed seismic data.

ACKNOWLEDGEMENT

REFERENCES

[1] A. Tarantola, "Inversion of seismic reflection data in the acoustic approximation," *Geophysics*, vol. 49, no. 8, pp. 1259–1266, 1984.

[2] J. Virieux and S. Operto, "An overview of full-waveform inversion in exploration geophysics," *Geophysics*, vol. 74, no. 6, pp. WCC1–WCC26, 2009.

[3] A. Klotzsche, J. van der Kruk, G. A. Meles, J. Doetsch, H. Maurer, and N. Linde, "Full-waveform inversion of cross-hole ground-penetrating radar data to characterize a gravel aquifer close to the thur river, switzerland," *Near surface geophysics*, vol. 8, no. 6, pp. 635–649, 2010.

[4] A. Klotzsche, H. Vereecken, and J. van der Kruk, "Gpr full-waveform inversion of a variably saturated soil-aquifer system," *J. Appl. Geophysics*, vol. 170, p. 103823, 2019.

[5] L. Guasch, O. Calderón Agudo, M.-X. Tang, P. Nachev, and M. Warner, "Full-waveform inversion imaging of the human brain," *NPJ Digit. Med.*, vol. 3, no. 1, p. 28, 2020.

[6] J. Rao, J. Yang, M. Ratassepp, and Z. Fan, "Multi-parameter reconstruction of velocity and density using ultrasonic tomography based on full waveform inversion," *Ultrasonics*, vol. 101, p. 106004, 2020.

[7] C. Shin and D.-J. Min, "Waveform inversion using a logarithmic wavefield," *Geophysics*, vol. 71, no. 3, pp. R31–R42, 2006.

[8] E. Bozdağ, J. Trampert, and J. Tromp, "Misfit functions for full waveform inversion based on instantaneous phase and envelope measurements," *Geophys. J. Int.*, vol. 185, no. 2, pp. 845–870, 2011.

[9] J. Luo and R.-S. Wu, "Seismic envelope inversion: reduction of local minima and noise resistance," *Geophys. Prospecting*, vol. 63, no. 3, pp. 597–614, 2015.

[10] B. Engquist and B. D. Froese, "Application of the wasserstein metric to seismic signals," *arXiv preprint arXiv:1311.4581*, 2013.

[11] L. Metivier, R. Brossier, Q. Mérigot, E. Oudet, and J. Virieux, "Measuring the misfit between seismograms using an optimal transport distance: application to full waveform inversion," *Geophys. J. Int.*, vol. 205, no. 1, pp. 345–377, 2016.

[12] M. Warner and L. Guasch, "Adaptive waveform inversion: Theory," *Geophysics*, vol. 81, no. 6, pp. R429–R445, 2016.

[13] A. Tikhonov, A. Goncharsky, V. Stepanov, and A. Yagola, *Numerical methods for the approximate solution of ill-posed problems on compact sets.* Springer, 1995.

[14] L. I. Rudin, S. Osher, and E. Fatemi, "Nonlinear total variation based noise removal algorithms," *Phys. D, Nonlinear Phenomena*, vol. 60, no. 1-4, pp. 259–268, 1992.

[15] K. Bredies, K. Kunisch, and T. Pock, "Total generalized variation," *SIAM J. Imag. Sci.*, vol. 3, no. 3, pp. 492–526, 2010.

[16] A. Asnaashari, R. Brossier, S. Garambois, F. Audebert, P. Thore, and J. Virieux, "Regularized seismic full waveform inversion with prior model information," *Geophysics*, vol. 78, no. 2, pp. R25–R36, 2013.

[17] A. Y. Anagaw and M. D. Sacchi, "Full waveform inversion with total variation regularization," in *Recovery-CSPG CSEG CWLS Convention*, 2011, pp. 1–4.

[18] S. Qu, E. Verschuur, and Y. Chen, "Full-waveform inversion and joint migration inversion with an automatic directional total variation constraint," *Geophysics*, vol. 84, no. 2, pp. R175–R183, 2019.

[19] Z. Du, D. Liu, G. Wu, J. Cai, X. Yu, and G. Hu, "A high-order total-variation regularisation method for full-waveform inversion," *J. Geophysics and Eng.*, vol. 18, no. 2, pp. 241–252, 2021.

[20] K. Gao and L. Huang, "Acoustic-and elastic-waveform inversion with total generalized p-variation regularization," *Geophys. J. Int.*, vol. 218, no. 2, pp. 933–957, 2019.

[21] E. Esser, L. Guasch, T. van Leeuwen, A. Y. Aravkin, and F. J. Herrmann, "Total variation regularization strategies in full-waveform inversion," *SIAM J. Imag. Sci.*, vol. 11, no. 1, pp. 376–406, 2018.

[22] E. Esser, L. Guasch, F. J. Herrmann, and M. Warner, "Constrained waveform inversion for automatic salt flooding," *Lead. Edge*, vol. 35, no. 3, pp. 235–239, 2016.

[23] P. Yong, W. Liao, J. Huang, and Z. Li, "Total variation regularization for seismic waveform inversion using an adaptive primal dual hybrid gradient method," *Inverse Problems*, vol. 34, no. 4, p. 045006, 2018.

[24] B. Peters, B. R. Smithyman, and F. J. Herrmann, "Projection methods and applications for seismic nonlinear inverse problems with multiple constraints," *Geophysics*, vol. 84, no. 2, pp. R251–R269, 2019.

[25] M. V. Afonso, J. M. Bioucas-Dias, and M. Figueiredo, "An augmented lagrangian approach to the constrained optimization formulation of imaging inverse problems," *IEEE Trans. Image Process.*, vol. 20, no. 3, pp. 681–695, 2011.

[26] G. Chierchia, N. Pustelnik, J.-C. Pesquet, and B. Pesquet-Popescu, "Epigraphical projection and proximal tools for solving constrained convex optimization problems," *Signal Image Video Process.*, vol. 9, no. 8, pp. 1737–1749, 2015.

[27] S. Ono and I. Yamada, "Signal recovery with certain involved convex data-fidelity constraints," *IEEE Trans. Signal Process.*, vol. 63, no. 22, pp. 6149–6163, 2015.

[28] S. Ono, "Primal-dual plug-and-play image restoration," *IEEE Signal Process. Lett.*, vol. 24, no. 8, pp. 1108–1112, 2017.

[29] S. Ono, "Efficient constrained signal reconstruction by randomized epigraphical projection," in *Proc. IEEE Int. Conf. Acoust., Speech, Signal Process., (ICASSP)*, 2019, pp. 4993–4997.

[30] B. Peters and F. J. Herrmann, "Constraints versus penalties for edge-preserving full-waveform inversion," *Lead. Edge*, vol. 36, no. 1, pp. 94–100, 2017.

[31] P. L. Combettes and N. N. Reyes, "Moreau's decomposition in banach spaces," *Math. Program.*, vol. 139, no. 1, pp. 103–114, 2013.

[32] A. Chambolle and T. Pock, "A first-order primal-dual algorithm for convex problems with applications to imaging," *J. Math. Imag. Vis.*, vol. 40, pp. 120–145, 2011.

[33] P. L. Combettes and J.-C. Pesquet, "Primal-dual splitting algorithm for solving inclusions with mixtures of composite, lipschitzian, and parallel-sum type monotone operators," *Set-Valued Var. Anal.*, vol. 20, no. 2, pp. 307–330, 2012.

[34] L. Condat, "A primal–dual splitting method for convex optimization involving lipschitzian, proximable and linear composite terms," *J. Optim. Theory Appl.*, vol. 158, no. 2, pp. 460–479, 2013.

[35] B. C. Vũ, "A splitting algorithm for dual monotone inclusions involving cocoercive operators," *Adv. Comput. Math.*, vol. 38, no. 3, pp. 667–681, 2013.

[36] R.-E. Plessix, "A review of the adjoint-state method for computing the gradient of a functional with geophysical applications," *Geophys. J. Int.*, vol. 167, no. 2, pp. 495–503, 2006.

[37] J. Duchi, S. Shalev-Shwartz, Y. Singer, and T. Chandra, "Efficient projections onto the l 1-ball for learning in high dimensions," in *Proceedings of the 25th international conference on Machine learning*, 2008, pp. 272–279.

[38] M. Louboutin, M. Lange, F. Luporini, N. Kukreja, P. A. Witte, F. J. Herrmann, P. Velesko, and G. J. Gorman, "Devito (v3. 1.0): an embedded domain-specific language for finite differences and geophysical exploration," *Geoscientific Model Develop.*, vol. 12, no. 3, pp. 1165–1187, 2019.